

Nanoscale Infrared Spectroscopy: Improving the Spectral Range of the Photothermal Induced Resonance Technique

Aaron M. Katzenmeyer,¹ Vladimir Aksyuk,¹ Andrea Centrone^{1,2}*

¹Center for Nanoscale Science and Technology, National Institute of Standards and Technology, Gaithersburg, MD 20899 (USA)

²Maryland Nanocenter, University of Maryland, College Park, MD 20742 (USA)

ABSTRACT

Photothermal Induced Resonance (PTIR) is a new technique which combines the chemical specificity of IR spectroscopy with the lateral resolution of Atomic Force Microscopy. PTIR requires a pulsed tunable laser for sample excitation and an AFM tip to measure the sample expansion induced by light absorption. The limited tunability of commonly available laser sources constrains the application of the PTIR technique to a portion of the IR spectrum. In this work, a broadly tunable pulsed laser relying on a difference frequency generation scheme in a GaSe crystal to emit light tunable from 1.55 μm to 16 μm (from 6450 cm^{-1} to 625 cm^{-1}) was interfaced with a commercial PTIR instrument. The result is a materials characterization platform capable of chemical imaging, in registry with atomic force images, with a spatial resolution that notably surpasses the light diffraction limit throughout the entire mid-IR spectral

range. PTIR nanoscale spectra and images allow the identification of compositionally and optically similar yet distinct materials; organic, inorganic, and composite samples can be studied with this nanoscale analog of infrared spectroscopy, suggesting broad applicability. Additionally, we compare the results obtained with the two tunable lasers, which have different pulse lengths, to experimentally assess the recently developed theory of PTIR signal generation.

MAIN TEXT

The engineering and application of nanomaterials in fields like electronics,¹ biology,² photovoltaics,³ and therapeutics^{4,5}, is a strong driver for improving the lateral resolution of many analytical techniques. For example, Fourier Transformed Infrared (FTIR) spectroscopy provides rich chemical and structural information,^{2,6,7} but the lateral resolution of FTIR microscopy⁸ is limited to several micrometers by the diffraction of the long IR wavelengths (3 μm to 20 μm).⁹⁻¹¹ To overcome these limitations a few nanoscale chemical imaging methods relying on scanning probe techniques have been proposed.¹²⁻¹⁶ The most commonly used among these techniques, scattering Scanning Near-field Optical Microscopy (s-SNOM)^{1,12,17,18} measures the light scattered by a sharp metallic tip when illuminated, typically, by a laser. The interaction of the IR light with the sample in the near field (enhanced by the proximity of the metallic tip) causes a change in the amplitude and phase of the scattered light as a function of both the local extinction coefficient (κ) and the real part of the refractive index (n).

However, since the signal is a complex function of n and κ the identification of unknown materials with a typical s-SNOM set up is a challenging task requiring theoretical modeling^{17,18} to describe the tip-sample-substrate interactions in the near field. In brief, data collected from

typical s-SNOM experiments are not directly comparable to spectra from IR spectroscopy. Recently a new s-SNOM set up that measures both the amplitude and phase of the scattered light using an asymmetric Michelson interferometer allowed computing s-SNOM spectra that, in good approximation, resemble far field FTIR spectra.¹⁶ However, it would be advantageous to obtain the IR spectra via direct absorption measurements and compare them with existing FTIR databases to identify the sample composition immediately, without additional computation; as demonstrated by the Photo Thermal Induced Resonance (PTIR) technique.^{19,20}

PTIR recently attracted great interest for enabling chemical identification and imaging with nanoscale resolution, combining the lateral resolution of Atomic Force Microscopy (AFM) with the chemical specificity of IR Spectroscopy.^{15,19,21-24} PTIR measures the transient thermal expansion induced by (pulsed) light absorption in the sample with an AFM tip in contact mode. Samples are placed on an optically transparent prism and illuminated from the bottom in a total internal reflection configuration to minimize the interaction of light with the AFM tip (Figure 1a). The absorption of a laser pulse in the sample results in local heating, sample expansion, and excitation of the AFM cantilever motion, which is monitored by reflecting the AFM laser beam from the cantilever onto a four-quadrant photodetector (fig. 1). The timescale of thermal expansion is much faster than the AFM feedback and is fast enough to excite several of the lowest-frequency mechanical modes of the cantilever (fig. 1c). The repetition frequency of the laser pulses (1 kHz) is slow enough to allow the cantilever to complete the ring down (Figure 1b) before a new pulse arrives. The infrared spectrum of the sample is obtained by plotting the maximum amplitude of the tip deflection (normalized by the laser power) as a function of wavelength. While the typical laser spot size is $\approx 30 \mu\text{m}$, the AFM tip acts as a spatial filter allowing the extraction of spectroscopic information with nanoscale resolution.^{19,22,23} Chemical

images can be obtained by illuminating the sample at a constant wavelength while scanning the AFM tip.^{22,23,25} Importantly, the PTIR signal is proportional to the energy absorbed²³ and PTIR spectra are directly comparable with FTIR spectral libraries^{19,20} allowing material identification. PTIR was used for chemical characterization with nanoscale resolution of bacteria,^{15,22} polymers,¹⁹ embedded quantum dots²⁶ and living cells.²⁷

The first demonstration of the PTIR technique was obtained using a broadly tunable free electron laser (FEL).²¹ Other tunable sources, like quantum cascade lasers²⁸ and optical parametric oscillators (OPOs)²⁰ have also been used in PTIR set-ups. Obviously, FELs offer the broadest tunability range but their high cost and limited availability makes them hardly accessible. Quantum cascade lasers are very promising in mid-IR applications but at the moment their tunability range is still limited to a few hundred cm^{-1} .^{28,29} The recent commercial availability of a PTIR set up using a broadly tunable OPO²⁰ as the laser source sparked great interest in this technique for nanoscale characterization.^{19,20,23} The typical OPOs used so far employ a ZnGeP_2 crystal to generate light continuously tunable from 2.5 μm to 9.09 μm (from 4000 cm^{-1} to \approx 1100 cm^{-1}) in 10 ns pulses with line widths between 5 cm^{-1} and 16 cm^{-1} . Recently this range was expanded to 900 cm^{-1} (11.11 μm); however, since good spectroscopy practice requires analyzing the positions of several absorption peaks for reliable chemical identification and because many inorganic materials are characterized by absorption at longer wavelengths, an extended spectral range is required for increasing the types of samples amenable to PTIR characterization.

In this work we describe the integration of a new broadly tunable laser with a commercial PTIR setup. The additional laser employs difference frequency generation (DFG) in a GaSe crystal to emit light tunable from 1.55 μm to 16 μm (from 6450 cm^{-1} to 625 cm^{-1}) with 0.5 cm^{-1}

spectral line width and 100 ps pulse duration. The extended wavelength range of the set-up is leveraged to analyze mixed polymer samples and silica nanoparticles. Initial theoretical considerations³⁰ suggested that, for a given laser pulse energy, shorter pulses should lead to a stronger PTIR signal. Later, a more refined model³¹ suggested that, for a given pulse energy, the PTIR signal should be independent on the laser pulse length as long as the sample relaxation time is much larger than the pulse length. In order to assess the theory we compare here PTIR spectra obtained with the ZnGeP₂ OPO (10 ns) and the new GaSe DFG laser (100 ps). Results show that the differences in PTIR spectra obtained with these laser pulses are negligible because the dynamics of the thermal expansion are essentially the same in both cases; both pulse lengths are for the sample, and therefore the AFM cantilever, instantaneous with respect to the characteristic thermal relaxation time and the period of the excited contact resonance modes, respectively. Based on this experimental observation we provide a conceptual framework useful for the analysis and optimization of PTIR transduction in future experiments.

EXPERIMENTAL SECTION

Experimental set up.

The simplified instrument scheme is presented in figure 2. PTIR experiments were carried out using a commercial PTIR set up which consists of an AFM microscope operating in contact mode and a tunable OPO laser source (Laser A in fig. 2). A second tunable laser system, hereafter laser B, was custom built by a commercial source and integrated by us with the commercial PTIR set up (fig 2). The light emitted by the lasers is linearly polarized and typically attenuated by a ZnSe wire grid polarizer (WGP) to control intensity at the sample. The sample is placed on a ZnSe prism and illuminated by total internal reflection. The laser light is focused

under the AFM tip with a ZnSe lens; the typical spot size is $30 \mu\text{m} \pm 10 \mu\text{m}$ depending on the wavelength. A power meter is used to record the laser light intensity as a function of wavelength (background spectrum) which is used to normalize the PTIR signal.

Laser A emits 10 ns pulses with a 1 kHz repetition rate and line widths between 5 cm^{-1} and 16 cm^{-1} depending on the wavelength. Laser A consists of a Q-switched diode pumped Nd:YAG laser (1064 nm), one OPO based on a periodically poled lithium niobate (PPLN) crystal and a second OPO based on a non-critically phase-matched ZnGeP₂ (ZGP) crystal. The Nd:YAG laser pumps the PPLN OPO which emits tunable light from $2.5 \mu\text{m}$ to $4.475 \mu\text{m}$. The light from the PPLN OPO is either used directly for the experiment or used as a pump for the ZGP OPO which yields continuously tunable output from $4.475 \mu\text{m}$ to $9.09 \mu\text{m}$.

Laser B emits 100 ps pulses with 0.5 cm^{-1} line width and a 1 kHz repetition rate. Laser B (fig. 2) consists of a mode-locked picosecond laser pump which provides a pulse train for driving a Synchronously-pumped Optical Parametric Oscillator (SOPO) and a single pulse for pumping an Optical Parametric Amplifier (OPA) and a Difference Frequency Generation (DFG) stages. The SOPO is designed such that the cavity round-trip time is matched to the inter-pulse spacing in the pulse train. The picosecond pump laser consists of three functional parts: master oscillator, continuous wave amplifier (Train amplifier) and regenerative amplifier. The master oscillator is a diode pumped mode-locked Nd:YVO₄ that has two output beams; the first is employed for seeding of the regenerative amplifier, the second beam is directed to a train amplifier based on a Nd:YVO₄ crystal laser rod in end pump geometry generating more than 6 W of output power at 87 MHz pulse repetition rate. The regenerative amplifier employs Pockels cells to select a single pulse from the master oscillator train and amplifies it to 2.5 mJ output energy at 1 kHz pulse repetition rate. The SOPO (pumped by 87 MHz train, fig. 2) has its cavity matched to the pump

inter-pulse spacing and is used for generating tunable radiation from 1.55 μm to 2.02 μm using a multi-grating PPLN crystal with period varying from 25.5 μm to 31.5 μm in 0.5 μm steps. The wavelength is tuned by using different poling periods and tuning dispersive intra-cavity components. The OPA (pumped by regenerative amplifier pulse output) consists of two angle-tuned KTiOAsO_4 (KTA) crystal sets. The pump pulse and the seed pulse from the SOPO signal train are temporally overlapped in the OPA stage by means of the built-in delay line. Two sets of KTA crystals are used to cover the whole tuning range. The first set of crystals has a tuning range from 1.652 μm to 2.02 μm (signal) and from 2.25 μm to 2.989 μm (idler); the second set of crystals has a tuning range from 1.55 μm to 1.651 μm (signal) and from 2.99 μm to 3.35 μm (idler). The mixing of the OPA signal and idler pulses in the GaSe crystal results in tunable radiation from 3.351 μm to 16.00 μm . The DFG design is based upon a single pass through a GaSe nonlinear crystal. Overall the laser system has a tunable output from 1.55 μm to 16.00 μm with 1 kHz repetition rate and energy per pulse up to 500 μJ . Dichroic mirrors or absorptive filters, depending on the wavelength, are used to cut unwanted spectral lines, so only a single wavelength is present at a time at the laser output.

Most of the optics in the PTIR set up and inside the lasers are placed on motorized stages which allow automatic wavelength selection and sweeping via a computer interface. Since different wavelengths are typically emitted by OPOs at different angles, an infrared pyroelectric camera was used to calibrate the mirror positions resulting in the laser output collinearity in the entire wavelength range. The laser beam was confined within an interlocked enclosure to avoid possible light exposure beyond the maximum permissible amount.

Sample preparation.

All chemicals were used as received without further purification.

Three samples (hereafter sample 1, sample 2, sample 3) were prepared for this study. Sample 1 consists of polymethylmethacrylate (PMMA) and polystyrene (PS) spherical particles embedded in an epoxy matrix. This sample was microtomed in thin slices and placed on a ZnSe ATR prism. The height of the epoxy matrix was $300 \text{ nm} \pm 10 \text{ nm}$ (as measured by AFM in different sample positions). For sample 2 an aqueous dispersion ($200 \mu\text{L}$) of 500 nm diameter COOH-functionalized silica spheres (50 mg/mL) was added to an anisole solution (12.5 mL) containing 6% PMMA by weight. To facilitate mixing, methanol (3.5 ml) was added drop wise, under stirring. The resulting solution was spin-cast onto a ZnSe prism at 50 Hz for 60 s using a custom made prism adaptor piece and baked (140° C for 5 min) to yield silica spheres in a PMMA matrix. The PMMA matrix ($250 \text{ nm} \pm 10 \text{ nm}$) prevents particle displacement by the AFM tip during imaging. Sample 3 is made of a monolayer of COOH-functionalized silica spheres (diameter 300 nm) obtained upon water evaporation after drop casting the silica aqueous dispersion (50 mg/mL) on the ZnSe prism.

PTIR measurements.

With the exception of the spectrum in figure 4 (spectrum not averaged) the PTIR spectra were recorded by averaging 4 consecutive spectra to increase the signal to noise ratio. Each individual spectrum was recorded by averaging the cantilever response from 256 individual laser pulses at each wavelength. A pyroelectric power meter is used to record the corresponding laser background spectrum which is used to normalize the PTIR signal intensity as a function of laser

power. PTIR images were recorded using the laser at a fixed wavelength by averaging 32 pulses per pixel. Pixel sizes are 20 nm x 20 nm unless otherwise noted.

Commercially available contact-mode AFM probes were used for this study. 450 μm long, 45 μm wide silicon probes with a nominal fundamental mode resonant frequency between 11 kHz and 21 kHz, and a nominal spring constant of 0.14 N/m up to 0.67 N/m were used for sample 1 and sample 2. 200 μm long, 30 μm wide silicon nitride probes with a nominal resonant frequency between 12 kHz and 28 kHz, and a nominal spring constant of 0.03 N/m to 0.24 N/m were used for samples 2 and 3. The nominal radius of curvature of the AFM probes used in this work was 6 nm and 10 nm for the silicon and silicon nitride cantilevers.

▪ RESULTS AND DISCUSSION

Sample 1 is used to demonstrate the chemical specificity and resolution of the PTIR technique. The PTIR spectra recorded at locations marked by the crosshairs in the AFM height image (figure 3a) show the characteristic absorption peaks of PMMA, PS and the epoxy respectively (figure 3g and h), allowing the identification of the composition of the different asperities observed in figure 3a. PTIR chemical images are acquired simultaneously with the AFM height image and allow mapping of the chemical composition with nanoscale resolution. For best correlation between the height and chemical image the AFM acquisition rate (pixels per second) should be equal to the PTIR acquisition rate defined as the laser repetition rate divided by the number of pulses averaged in generating each pixel²³ (32 in this work). Consecutive PTIR images (pixel size 25 nm x 25 nm) were acquired at 694 cm^{-1} (14.41 μm), 825 cm^{-1} (12.12 μm), 1142 cm^{-1} (8.76 μm), 1721 cm^{-1} (5.81 μm) and 3030 cm^{-1} (3.30 μm) and are reported in fig. 3b-f. The absorption at 694 cm^{-1} and 3030 cm^{-1} corresponds to the C-H out of plane bending and

aromatic C-H stretching of PS, respectively. The absorption at 825 cm^{-1} is assigned to aromatic C-H out of plane bending in the epoxy. The absorptions at 1142 cm^{-1} and 1721 cm^{-1} in PMMA are assigned to a vibration involving C-O stretching and C-O-H bending and to carbonyl stretching, respectively.³² The height image allows the identification of only three particles, but the PTIR images reveal the existence of one PMMA particle (figure 3 c and d) and four PS particles (figure 3b and f). Two of the PS particles lay either on top or underneath the larger PMMA particle.

Notably, the lateral resolution of the PTIR images does not depend on the wavelength. This is an important characteristic because it allows chemical imaging of the components of a heterogeneous mixture with the same lateral resolution, something impossible in diffraction limited experiments like FTIR microscopy in which the lateral resolution is a function of wavelength. The extended wavelength range of laser B allows the unequivocal identification of PS particles' location, otherwise difficult because of the reduced chemical contrast with the other materials in sample 1 in the spectral region above 1000 cm^{-1} , as reported previously²³ (see also fig. 3g where a PMMA peak partially overlaps with the PS vibration at 3030 cm^{-1}).

Figure 4 shows the AFM height image (a) and PTIR chemical map (1095 cm^{-1} , b) of a 500 nm silica sphere in a PMMA matrix (sample 2); the PTIR map exhibits sharp chemical contrast at the boundary between the particle and matrix and good spatial correlation with the AFM height image as can be seen by the height and PTIR line profiles across the sphere (figure 4c). This is the first experimentally validated display of PTIR's ability to perform nanoscale characterization of inorganic materials (i.e. the AFM image provides independent confirmation of the single particle's spatial extent). In fact, the only two previous studies where PTIR was applied to study inorganic materials invoked statistical means to identify buried quantum dots^{26,33} and no direct

correlation could be made with the topographic image. PTIR spectra collected on individual silica particles in the PMMA matrix show a peak at 1100 cm^{-1} attributed to Si-O stretching, as shown in figure 4d.

According to the PTIR theory developed by Dazzi³¹ the PTIR signal should be proportional to the sample's linear expansion coefficient (α) and inversely proportional to its thermal conductivity (η). Imaging silica with the PTIR technique is certainly harder than measuring polymeric samples which are typically characterized by large α and small η .³⁴ Recently, we used the PTIR technique to measure PMMA samples as thin as 40 nm,²³ here we note that silica particles as small as 300 nm, the thinnest sample tested, are measurable (see fig. S-1 of the supporting info). Despite the challenges imposed on AFM imaging (easy displacement of the silica particles by the AFM tip), no polymer matrix was employed on the third sample studied to ensure the signal originated exclusively from the inorganic material. Silicon nitride probes were used for sample 3 because they exhibited superior response to large and abrupt topographical variations. While the α/η ratio for silica is approximately 300 times smaller than for PS, the silica melting point is much higher than PS which can be leveraged to generate a measurable signal. For example, the signal to noise ratio for the PS spectra in fig 3f is 120:1, and for the silica spectra in fig. 4d it is 20:1.

For a given pulse energy, theoretical considerations^{30,31} have suggested a different dependence of the PTIR signal with respect to the laser pulse length. The different pulse lengths of the lasers employed in this work (100 ps and 10 ns) are used to experimentally test the theories and to derive practical considerations for the design of future experiments. For a given sample the expression derived by Dazzi et al.³⁰ predicts a PTIR signal 100 times stronger for 100 ps excitation. After normalizing for the pulse energy, the results of a later paper³¹ suggest that the

PTIR signal should be independent of the laser pulse length for pulses much shorter than the relaxation time. A PMMA microtomed sphere of radius $\approx 1.3 \mu\text{m}$ and thickness 360 nm embedded in the epoxy matrix (sample 1) was chosen for the comparison (see the fig. 5a inset). Figure 5a shows the absorption intensity of the 1140 cm^{-1} and 1265 cm^{-1} peaks of PMMA normalized by the incident laser power. Despite the duration of the pulse varying by two orders of magnitude (10 ns for laser A, 100 ps for laser B), the spectra obtained with different pulse lengths have comparable intensities (i.e. \ll the two orders of magnitude difference initially predicted).³⁰ We can understand this as follows.

In PTIR the signal is generated through the following transduction chain: optical energy into heat, heat into mechanical thermal expansion, thermal expansion into cantilever motion, and cantilever motion into the photodetector signal. All these transduction stages should be considered to optimize the technique's performance (sensitivity, lateral resolution, etc.). The recorded signal can be understood by describing the transduction as a series of linear filters where the output of each stage is a convolution of the input signal with the impulse response of the stage. A detailed treatment of this transduction chain is beyond the scope of this work and it will be described elsewhere. In the experiments reported here, since laser pulse lengths are much shorter than the characteristic timescale of the thermal response, the measured signal is determined by the impulsive thermal response filtered by the harmonic responses of the cantilever modes weighted by the optical sensitivity of the detector to each mode.

In general, determining the spatial and temporal evolution of the temperature increase and consequent thermal expansion can be quite complex for inhomogeneous samples in terms of thickness, optical absorption, specific heat capacity, thermal conductivity, etc. Here we will consider the sample to be locally homogeneous in composition and physical geometry and

illuminated by a laterally uniform beam. Since the thermal conductivity and particularly the heat capacity of the ZnSe prism are much larger than those of the PMMA sample, we assume that the prism temperature does not change significantly. We note that the temporal cooling dynamic is thickness-dependent (even in case of uniform volumetric heating) and is not simply described by a single exponential. However, the longest characteristic thermalization timescale is of the order t_{relax} ,

$$t_{relax} \approx \frac{\rho \cdot C_p \cdot z^2}{\eta} \quad (1)$$

where ρ is the density, C_p is the specific heat capacity, η is the thermal conductivity and z is the thickness of the film. This timescale can be even longer if an interfacial thermal barrier between PMMA and the ZnSe prism is present and significant. For our sample $t_{relax} \approx 1 \mu s$, much longer than the pulse lengths for both lasers and much longer than the timescale for the conversion of optical power into heat.

While not entirely accurate, it is instructive to consider a simple lumped, low-pass filter model for the temporal evolution of the film temperature *averaged over the film thickness* during and after a single laser pulse. This assumes that the temperature is exponentially relaxing toward an equilibrium temperature with a single time scale, resulting in:

$$T(t) = T_0 + \begin{cases} \frac{T_{max}}{\left(1 - \exp\left(-\frac{t_1}{t_{relax}}\right)\right)} \cdot \left(1 - \exp\left(-\frac{t}{t_{relax}}\right)\right), & 0 < t < t_1 \\ T_{max} \cdot \exp\left(-\frac{t-t_1}{t_{relax}}\right), & t_1 < t \end{cases}, \quad (2)$$

where T_0 is the prism temperature, T_{max} is the maximum average temperature reached by the film at $t=t_1$ and t_1 is the laser pulse duration.

Changes in the temperature induce local stresses due to thermal expansion, which in turn result in the mechanical motion of the film and the cantilever. In the absence of the cantilever, the film thickness would be tracking the equilibrium thickness given by the time dependent temperature:

$$z(t) = z_0(1 + \alpha(T(t) - T_0)), \quad (3)$$

where z_0 is the initial material thickness, and α is the linear coefficient of thermal expansion.

This thermal expansion is mechanically equivalent to an isothermal application of a time dependent force to the film-cantilever interface:

$$F(t) = k_0 z(t), \quad (4)$$

where k_0 is the film's effective stiffness. This force excites the cantilever motion, which can be described in the modal basis, where each mode is an independent harmonic oscillator, typically with a reasonably high quality factor (Q). Consequently, each mode will filter the applied time dependent forcing function and respond most significantly only to the narrow portion of the excitation spectrum centered on the resonance frequency of that mode. Finally, that response is weighted by the sensitivity of the optical readout, which is proportional to the cantilever tilt angle at the location of the AFM laser spot.

Since the PTIR spectra are obtained after normalizing for the laser power, hereafter we will compare pulses with the same energy and different pulse length. Since the sample under investigation has $t_{\text{relax}} \approx 1 \mu\text{s}$, a negligible heat loss occurs for both 10 ns and 100 ps pulse durations. Therefore, the T_{max} reached using laser A and laser B are nearly identical (for a given energy per pulse). The forcing functions applied to the cantilever have a temporal extent dominated by t_{relax} and essentially the same maximum value, differing only in the rise time to T -

\max . Since the higher order modes of the cantilever have larger spring constants, only the cantilever's lower order modes contribute significantly to the measured signal (see e.g. Fig. 1c). The periods of these cantilever modes are orders of magnitude slower than even the 10 ns rise time generated by laser A. For the modes contributing to the signal, the forcing function appears as an “instantaneously” applied impulsive loading of similar magnitude and duration for both laser A and B. Given the AFM laser position was unchanged throughout the collection of data for Fig. 5, we arrive at the conclusion that the difference in the spectra generated by laser A and laser B should be negligible for this sample, as observed experimentally. In general, the PTIR signal is expected to be independent on the laser pulse length for all cases where thermalization time (t_{relax}) is much longer than the duration of the laser pulse. This may not be true in instances where the laser pulse length approaches the sample thermal relaxation and/or the tip mechanical response timescales. While those cases can also be analyzed following the linear transduction chain framework outlined above, such analysis is beyond the scope of this paper.

In summary a broadly tunable laser was integrated with a commercial PTIR instrument resulting in a platform suitable for nanoscale spectroscopy on a full range of organic and inorganic samples. Our experiments support the predictions of the recently refined PTIR theory proposed by Dazzi³¹ and show that the effect of the pulse duration in generating the PTIR signal needs to be considered with respect to the forcing function imparted on the cantilever. Additionally, we believe that the improved spectral resolution (0.5 cm^{-1}), 20 times better than the previously used OPO, will provide enhanced contrast for nanoscale chemical imaging of materials with partial spectral overlap and it will enable the determination of small spectral shifts expected for temperature dependent PTIR experiments.

Supporting Information. AFM, PTIR image and spectrum of 300 nm silica particles (sample 3) are available free of charge via the Internet at <http://pubs.acs.org>

AUTHOR INFORMATION

Corresponding Author

* e-mail: andrea.centrone@nist.gov, phone: 301-975-8225.

Author Contributions

The manuscript was written through contributions of all authors. All authors have given approval to the final version of the manuscript.

ACKNOWLEDGMENT

The authors acknowledge Kevin Kjoller of Anasys Instruments for providing the microtomed sample and Lucian Hand of Altos Photonics for the useful discussion on the laser systems. A. C. acknowledges support from the National Institute of Standards and Technology American Recovery and Reinvestment Act Measurement Science and Engineering Fellowship Program, Award 70NANB10H026, through the University of Maryland. A. C. acknowledges support under the Cooperative Research Agreement between the University of Maryland and the National Institute of Standards and Technology Center for Nanoscale Science and Technology, Award 70NANB10H193, through the University of Maryland.

- (1) Huber, A. J.; Wittborn, J.; Hillenbrand, R. *Nanotechnology* **2010**, *21*, 235702
- (2) Fernandez, D. C.; Bhargava, R.; Hewitt, S. M.; Levin, I. W. *Nature Biotechnology* **2005**, *23*, 469-474.
- (3) Nicholson, P. G.; Castro, F. A. *Nanotechnology* **2010**, *21*, 492001.
- (4) Park, J. H.; von Maltzahn, G.; Ong, L.; Centrone, A.; Hatton, T. A.; Ruoslahti, E.; Bhatia, S. N.; Sailor, M. J. *Advanced Materials* **2009**, *22*, 880-885.
- (5) Zhang, L. J.; Webster, T. J. *Nano Today* **2009**, *4*, 66-80.

- (6) Centrone, A.; Hu, Y.; Jackson, A. M.; Zerbi, G.; Stellacci, F. *Small* **2007**, *3*, 814-817.
- (7) Rao, G. R.; Castiglioni, C.; Gussoni, M.; Zerbi, G.; Martuscelli, E. *Polymer* **1985**, *26*, 811-820.
- (8) Bhargava, R. *Applied Spectroscopy* **2012**, *66*, 1091-1120.
- (9) Petibois, C.; Piccinini, M.; Guidi, M. C.; Marcelli, A. *Journal of Synchrotron Radiation* **2010**, *17*, 1-11.
- (10) Nasse, M. J.; Walsh, M. J.; Mattson, E. C.; Reiningger, R.; Kajdacsy-Balla, A.; Macias, V.; Bhargava, R.; Hirschmugl, C. J. *Nature Methods* **2011**, *8*, 413-U458.
- (11) Reddy, R. K.; Walsh, M. J.; Schulmerich, M. V.; Carney, P. S.; R., B. *Applied Spectroscopy* **2013**, *67*, 93-105.
- (12) Knoll, B.; Keilmann, F. *Nature* **1999**, *399*, 134-137.
- (13) Hillenbrand, R.; Taubner, T.; Keilmann, F. *Nature* **2002**, *418*, 159-162.
- (14) Bozec, L.; Hammiche, A.; Pollock, H. M.; Conroy, M.; Chalmers, J. M.; Everall, N. J.; Turin, L. *Journal of Applied Physics* **2001**, *90*, 5159-5165.
- (15) Dazzi, A.; Prazeres, R.; Glotin, F.; Ortega, J. M. *Ultramicroscopy* **2007**, *107*, 1194-1200.
- (16) Huth, F.; Govyadinov, A.; Amarie, S.; Nuansing, W.; Keilmann, F.; Hillenbrand, R. *Nano Letters* **2012**, *12*, 3973-3978.
- (17) Knoll, B.; Keilmann, F. *Optics Communications* **2000**, *182*, 321-328.
- (18) Cvitkovic, A.; Ocelic, N.; Hillenbrand, R. *Optics Express* **2007**, *15*, 8550-8565.
- (19) Marcott, C.; Lo, M.; Kjoller, K.; Prater, C.; Noda, I. *Applied Spectroscopy* **2011**, *65*, 1145-1150.
- (20) Kjoller, K.; Felts, J. R.; Cook, D.; Prater, C. B.; King, W. P. *Nanotechnology* **2010**, *21*, 185705.
- (21) Dazzi, A.; Prazeres, R.; Glotin, E.; Ortega, J. M. *Optics Letters* **2005**, *30*, 2388-2390.
- (22) Dazzi, A.; Prazeres, R.; Glotin, F.; Ortega, J. M.; Al-Sawaftah, M.; de Frutos, M. *Ultramicroscopy* **2008**, *108*, 635-641.
- (23) Lahiri, B.; Holland, G.; Centrone, A. *Small* **2012**, *10*.1002/sml.201200788.
- (24) Dazzi, A.; Prater, C. B.; Hu, Q. C.; Chase, D. B.; Rabolt, J. F.; Marcott, C. *Applied Spectroscopy* **2012**, *66*, 1365-1384.
- (25) Felts, J. R.; Kjoller, K.; Lo, M.; Prater, C. B.; King, W. P. *Acs Nano* **2012**, *6*, 8015-8021.
- (26) Sauvage, S.; Driss, A.; Reveret, F.; Boucaud, P.; Dazzi, A.; Prazeres, R.; Glotin, F.; Ortega, J. M.; Miard, A.; Halioua, Y.; Raineri, F.; Sagnes, I.; Lemaitre, A. *Physical Review B* **2011**, *83*, 035302.
- (27) Mayet, C.; Dazzi, A.; Prazeres, R.; Allot, E.; Glotin, E.; Ortega, J. M. *Optics Letters* **2008**, *33*, 1611-1613.
- (28) Lu, F.; Belkin, M. A. *Optics Express* **2011**, *19*, 19942-19947.
- (29) Hugi, A.; Terazzi, R.; Bonetti, Y.; Wittmann, A.; Fischer, M.; Beck, M.; Faist, J.; Gini, E. *Applied Physics Letters* **2009**, *95*.
- (30) Dazzi, A. In *Thermal Nanosystems and Nanomaterials*; Volz, S., Ed. 2009; Vol. 118, p 469-503.
- (31) Dazzi, A.; Glotin, F.; Carminati, R. *Journal of Applied Physics* **2010**, *107*, 124519
- (32) *handbook of infrared and raman characteristic frequencies of organic molecules*; Lin-Vien, D.; Colthup, N. B.; Fately, W. G.; Grasselli, J. G., Eds.; Academic Press: Boston, 1991.
- (33) Houel, J.; Sauvage, S.; Boucaud, P.; Dazzi, A.; Prazeres, R.; Glotin, F.; Ortega, J. M.; Miard, A.; Lemaitre, A. *Physical Review Letters* **2007**, *99*.
- (34) *Physical Properties of Polymer Handbook*; first ed.; Mark, J. E., Ed.; AIP press: Woodbury NY, 1996.

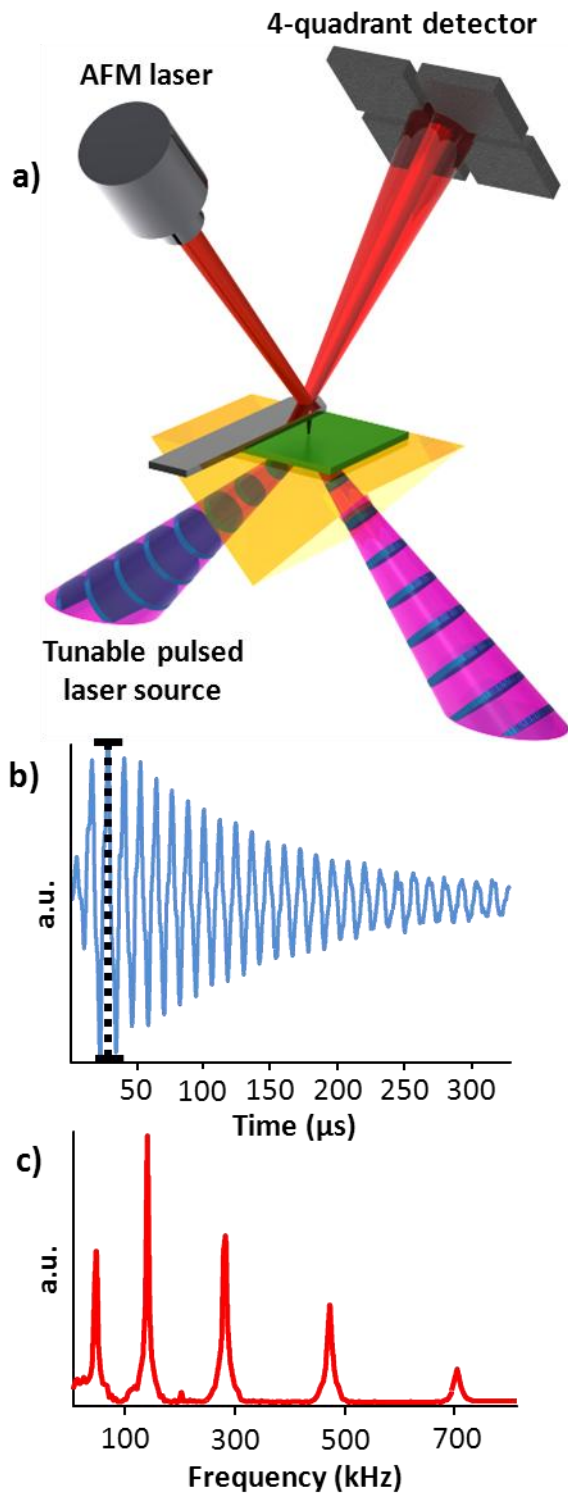


Figure 1. (a) Illustration of the PTIR measurement: if the sample absorbs the IR laser pulses (blue discs in purple cones) it rapidly expands deflecting the AFM cantilever which is monitored

by a four-quadrant detector. (b) The maximum peak to peak deflection during the cantilever ring down is proportional to the optical energy absorbed and it is used to generate the PTIR signal. The sample and cantilever have enough time to return to equilibrium before being excited by a new pulse. (c) By Fourier transformation of a ring down signal it is possible to obtain the amplitude of the different contact resonance modes excited by the sample expansion.

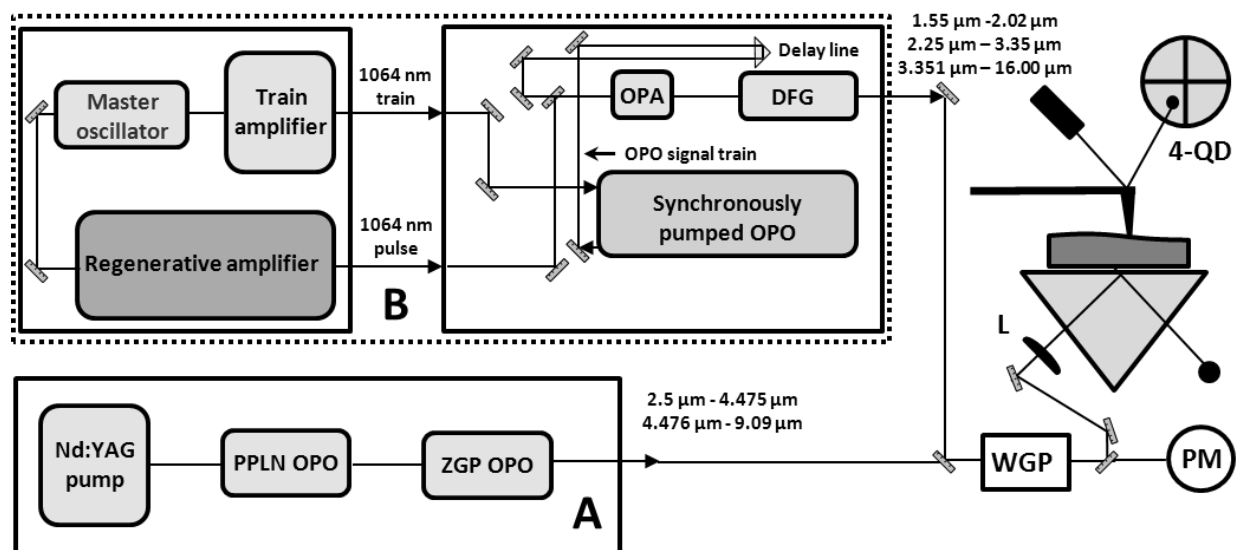


Figure 2. Simplified schematic of the PTIR set up used in this work. The light emitted by two tunable laser sources (A, B) is attenuated by a wire grid polarizer (WGP) and focused under the AFM tip by a ZnSe lens (L). A power meter (PM) is used to record the laser background spectrum used to normalize the PTIR signal recorded by the AFM four-quadrant detector (4-QD). In laser A is a Q-switched diode pumped Nd:YAG laser, pumps a PPLN OPO which pumps a ZGP OPO yielding a continuously tunable output from 2.5 μm to $\approx 9.09 \mu\text{m}$. In laser B, the master oscillator has two output beams that are used to pump a train amplifier and to seed the regenerative amplifier. The light emitted by the regenerative amplifier (pulse) is combined with the light emitted by a synchronously pumped OPO (train) inside an optical parametric amplifier (OPA) based on two sets of KTA crystals. A built-in delay line ensures the temporal overlap of the 2 beams. The signal and idler beam from the OPA can be either used in the PTIR experiment or can be mixed in a non-linear GaSe crystal to generate tunable output via difference frequency generation (DFG). Laser B yields tunable light between 1.55 and 16 μm . The schematic is intended for illustrative purposes only and doesn't reflect the exact location or size of the optical components used.

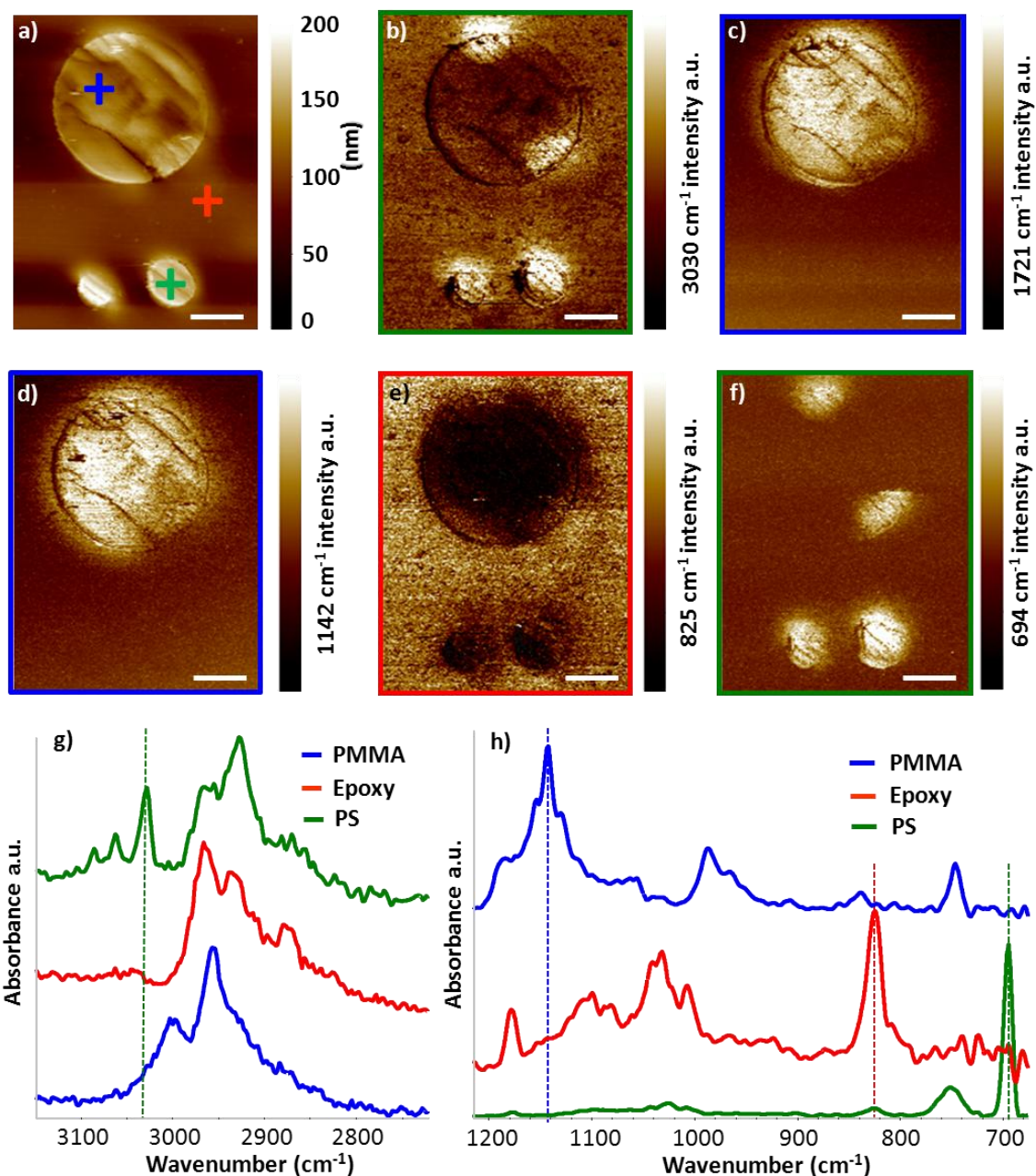


Figure 3. Sample 1 AFM height image (a), PTIR chemical images (b-f) and PTIR spectra (g, h) recorded at the locations marked “+” in panel a. The PTIR spectra were recorded by tuning the laser wavelength at 3 cm^{-1} interval. While the height image allows identifying the location of only three particles, the PTIR images and spectra not only reveal the location of 5 particles but allow the identification of the particles’ chemical nature. The PTIR images recorded at 1721 cm^{-1}

(c) and 1142 cm^{-1} (d) reveal the position of a PMMA particle. The PTIR image recorded at 825 cm^{-1} identifies the epoxy matrix (e). The position of 4 PS particles is revealed by the images recorded at 3030 cm^{-1} (b) and 694 cm^{-1} (f). All scale bars are $1\text{ }\mu\text{m}$. Figures b, c, and g were collected using laser A. Figures d, e, and h were collected using laser B.

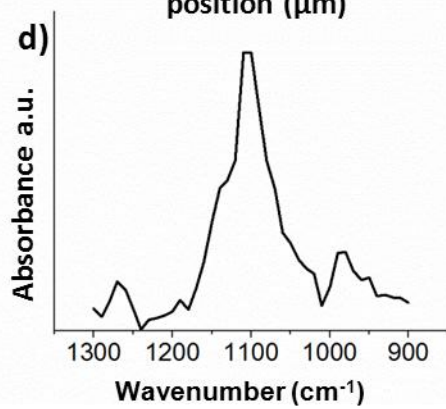
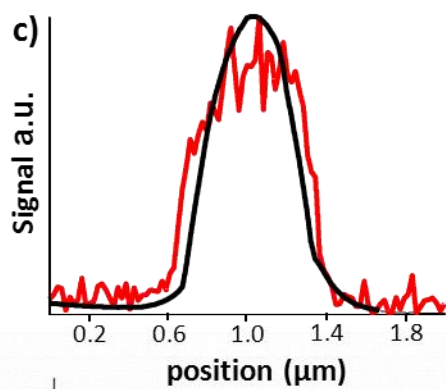
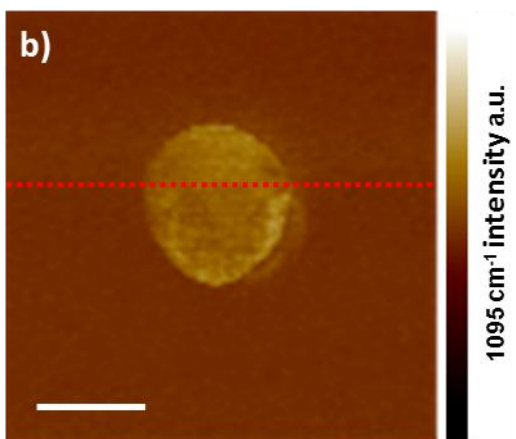
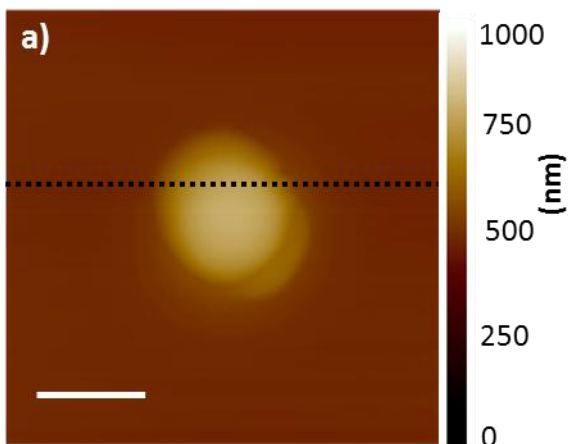


Figure 4. Sample 2 (silica sphere in PMMA matrix) AFM height image (a) and PTIR chemical map obtained by illuminating the sample at 1095 cm^{-1} typical of silica Si-O stretching (b). Scale bars are 500 nm. (c) Normalized line profiles for height (black) and 1095 cm^{-1} PTIR intensity signal (red) taken along the dashed lines shown in panels a and b. (d) Representative PTIR spectrum of a single silica particle in PMMA collected by tuning the laser at intervals of 10 cm^{-1} ; The smaller peaks at 984 cm^{-1} and 1264 cm^{-1} are attributed to the partially underlying PMMA matrix.

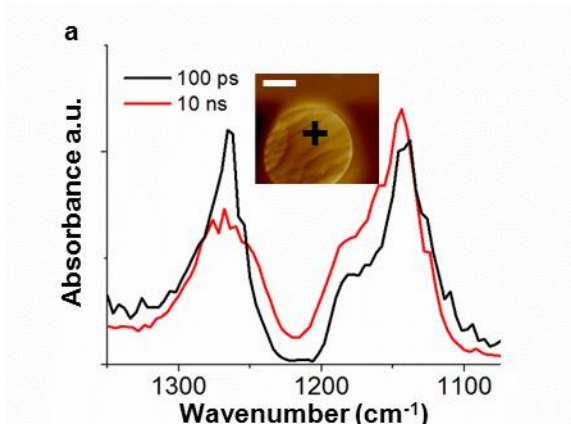


Figure 5. (a) PTIR spectra collected on a PMMA particle (sample 1) using 10 ns (red) and 100 ps (black) pulse lengths and tuning each laser at an interval of 4 cm^{-1} . The inset shows the AFM height image of the PMMA particle used for the comparison; the scale bar is $1\text{ }\mu\text{m}$. The PTIR spectra were taken in the location marked “+” and are normalized with respect to the laser power used in the experiments. The laser power ratio between laser A and laser B, was 0.12 and 1.43 for the 1140 cm^{-1} and 1265 cm^{-1} peaks, respectively.

Supporting information for:

Nanoscale Infrared Spectroscopy: Improving the Spectral Range of the Photothermal Induced Resonance Technique

Aaron M. Katzenmeyer,¹ Vladimir Aksyuk,¹ Andrea Centrone^{1,2*}

¹Center for Nanoscale Science and Technology, National Institute of Standards and Technology, Gaithersburg, MD 20899 (USA)

²Maryland Nanocenter, University of Maryland, College Park, MD 20742 (USA)

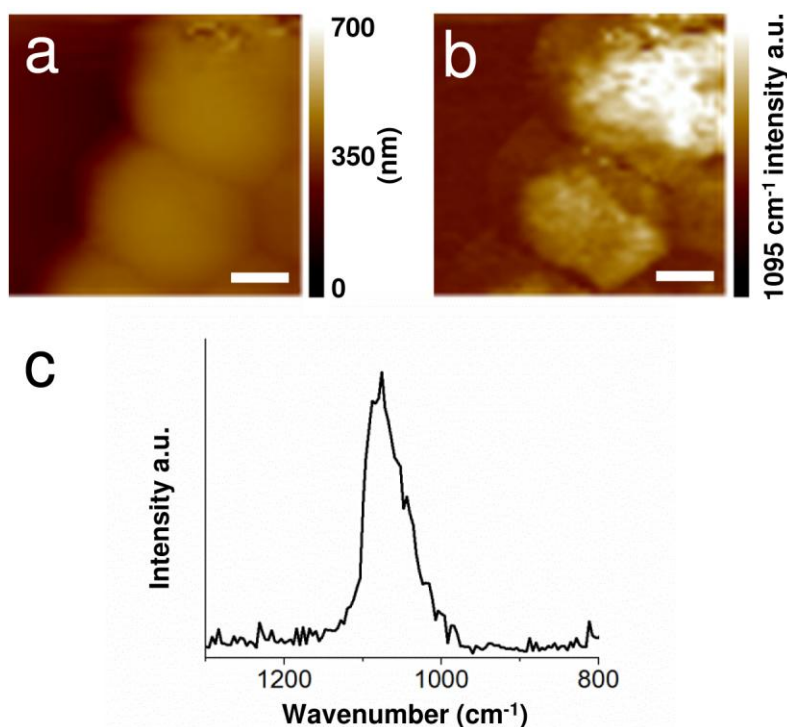


Figure S-1. a) AFM height image, b) 1095 cm⁻¹ PTIR chemical map and c) PTIR spectrum for silica spheres deposited directly onto a ZnSe prism (sample 3). Scale bars are 200 nm. The PTIR spectrum was recorded by tuning the laser at an interval of 4 cm⁻¹.